Influence of niobium and hafnium doping on the wear and corrosion resistance of coatings based on ZrN

Tao He [a,*], Zhylinski Valery [b], Alexey Vereschaka [c], Anthon Keshin [b], Yuanming Huo [a,**], Filipp Milovich [d], Catherine Sotova [e], Anton Seleznev [e]

[a] *School of Mechanical and Automotive Engineering, Shanghai University of Engineering Science, No. 333 Longteng Road, Shanghai, China*
[b] *Department of Chemistry, Technology of Electrochemical Production and Electronic Engineering Materials, Chemical Technology and Engineering Faculty, Belarusian State Technological University, 13a, Sverdlov Street, 220006, Minsk, Belarus*
[c] *Institute of Design and Technological Informatics of the Russian Academy of Sciences (IDTI RAS), Vadkovsky per. 18-1a, 127994, Moscow, Russia*
[d] *Materials Science and Metallurgy Shared Use Research and Development Center, National University of Science and Technology MISiS, Leninsky Prospect 4, 119049, Moscow, Russia*
[e] *Department of High-Efficiency Machining Technologies, Moscow State Technological University STANKIN, Vadkovsky per. 1, 127994, Moscow, Russia*

ARTICLE INFO

ABSTRACT

The properties of coatings based on the ZrN system with the introduction of hafnium and zirconium (ZrN, (Zr,Nb)N and (Zr,Hf)N), deposited on a Ti6Al–4V titanium alloy substrate are compared. Coatings are deposited by controlled accelerated arc-physical vapor deposition, and the structure of the coatings is studied using a transmission electron microscope. A comparison is made of both the mechanical (hardness, wear resistance, scratch strength) and anticorrosion (in a 3 % solution of NaCl) properties. The (Zr,Hf)N coating (22 at% Hf and 78 at% Zr) has the maximum hardness (HV, 3225 ± 73) and wear resistance. This coating also exhibits higher corrosion resistance. In contrast, introducing Nb into the coating composition reduces the corrosion resistance. This combination of beneficial properties makes the (Zr,Hf)N coating useful for conditions in which the surfaces of parts must simultaneously have high wear resistance, strength, and corrosion resistance.

1. Introduction

In modern mechanical engineering, applications can often require materials that simultaneously have high strength, wear resistance, and corrosion resistance. In particular, we can consider friction pairs operating in aggressive environments (for example, in seawater or the environment of the human body – implants). Functional coatings can be applied to help bulk materials meet these requirements.

Coatings based on the ZrN system are widely used in various fields because of their high hardness and wear resistance, as well as their beneficial anticorrosion properties [1–5]. The hardness of the ZrN coating can reach 32.2 GPa [6] and can be increased further by introducing additional elements such as hafnium (Hf) and niobium (Nb) [7–12]. ZrN coatings have a cubic structure with a predominant orientation (200) and a symmetrical state of residual compressive stresses [13,14]. An increase in the mechanical properties of ZrN systems is

attributed to the increase in defects and deformation of the Zr lattice during the introduction of nitrogen into the interstitial space and the formation of a new ZrN phase [15]. In addition to face-centered cubic ZrN, a wurtzite (w-ZrN) phase, as well as two-dimensional (2D) and three-dimensional (3D) forms of a layered hexagonal (h-ZrN) phase can theoretically form [16]. Moreover, the wear resistance of the ZrN coating depends on the nitrogen pressure during deposition [17–19], and the deposition temperature has a noticeable effect on the property of the coating [20,21]. The concentration of vacancies and other structural defects in the ZrN coating material decreases with increasing deposition temperature [20]. ZrN coatings also exhibit high crack resistance and brittle fracture resistance [22–27]. The crack resistance and fracture strength of the coating can be associated with the accumulation and relaxation of residual stresses during deposition [23]. The high heat resistance of the coating manifests in the preservation of the structure parameters during long-term holding at a temperature of 1000 °C [28].

Table 1
Composition of the Ti6Al–4V alloy, wt%.

Element	V	Al	Ti
Content, wt%	2.76 ± 2.14	7.48 ± 1.73	89.75 ± 2.81

The thickness of the metal layer in the two-layer ZrN/Zr coating, which is optimal from the point of view of energy removal efficiency, is approximately 100 nm [29].

The introduction of additional elements, particularly Hf and Nb, makes it possible to alter the properties of the ZrN coating. The presence of Hf in the coating composition, even in a small amount (1.8–2.7 at%), leads to a noticeable increase in hardness [7,9]. The introduction of 11.9 at% Hf into the ZrN coating does not significantly affect the level of residual stresses; however, the hardness and Young's modulus increase in this case [8]. The introduction of Hf (21 at%) makes it possible to increase the wear resistance of the coating [30,31]. At the appropriate concentration, the complete dissolution of Hf in ZrN is observed, with the formation of a solid solution. Alternatively, a decrease in the coating hardness and grain growth occurs upon the addition of 0.5–4.2 at% Hf [32]. Finally, the Zr, Hf adhesive layer can be modified, which may affect the properties of a coating based on the (Zr,Hf)N system [33–36].

The deposition of a ZrN coating provides effective protection against corrosion [37]. In particular, the ZrN coating deposited on the Ti6Al–4V substrate provides high corrosion resistance in saline physiological solution and high bioadhesion resistance of *Staphylococcus aureus* bacteria [38]. ZrN coatings have also shown anticorrosion properties in simulated body fluid (SBF) [39], physiological NaCl solution [40,41], and
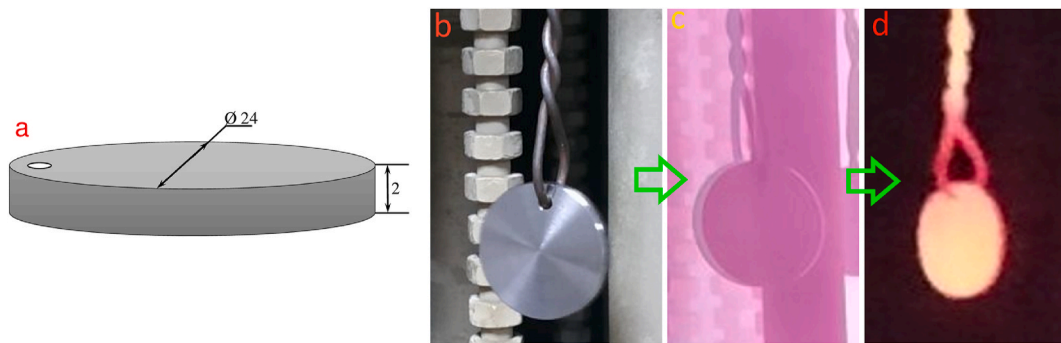
Fig. 1. Shape and dimensions (mm) of specimens. (a) Shape and dimensions of samples, Coating sequence: (b) fixing the sample on the tooling, (c) ion etching of the sample, and (d) coating deposition.
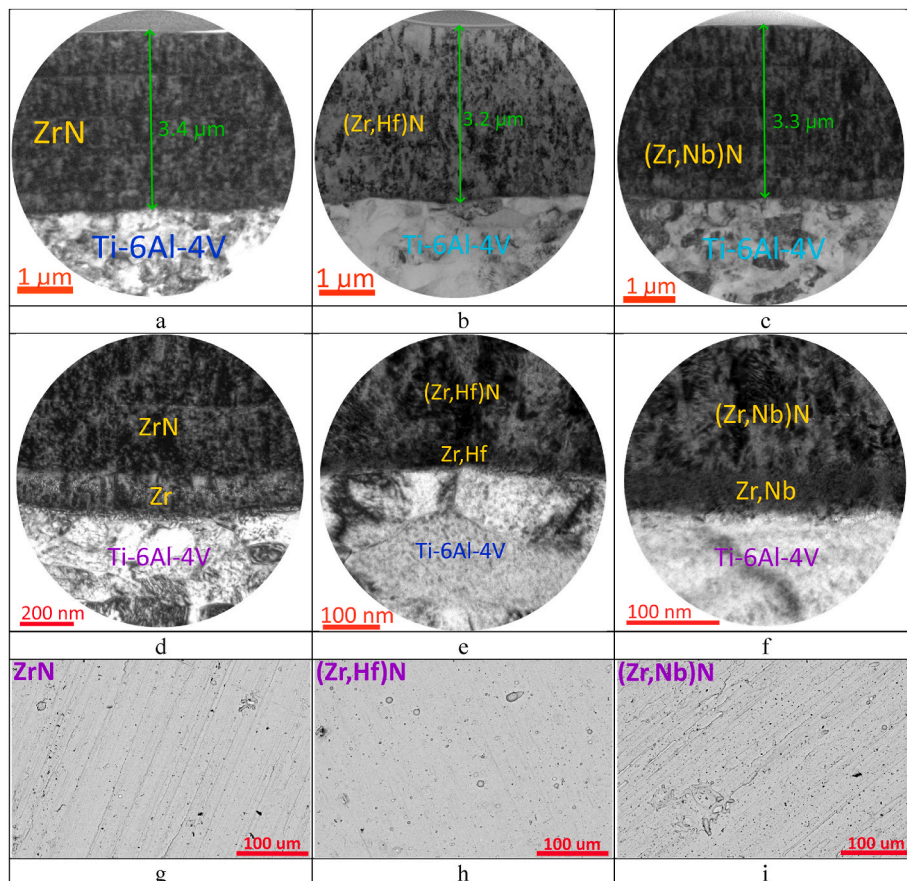
Fig. 2. (a–c) General structure of coatings, (d–f) structure of the interface between the coating and the substrate, (g–i) surface morphology of coated samples.
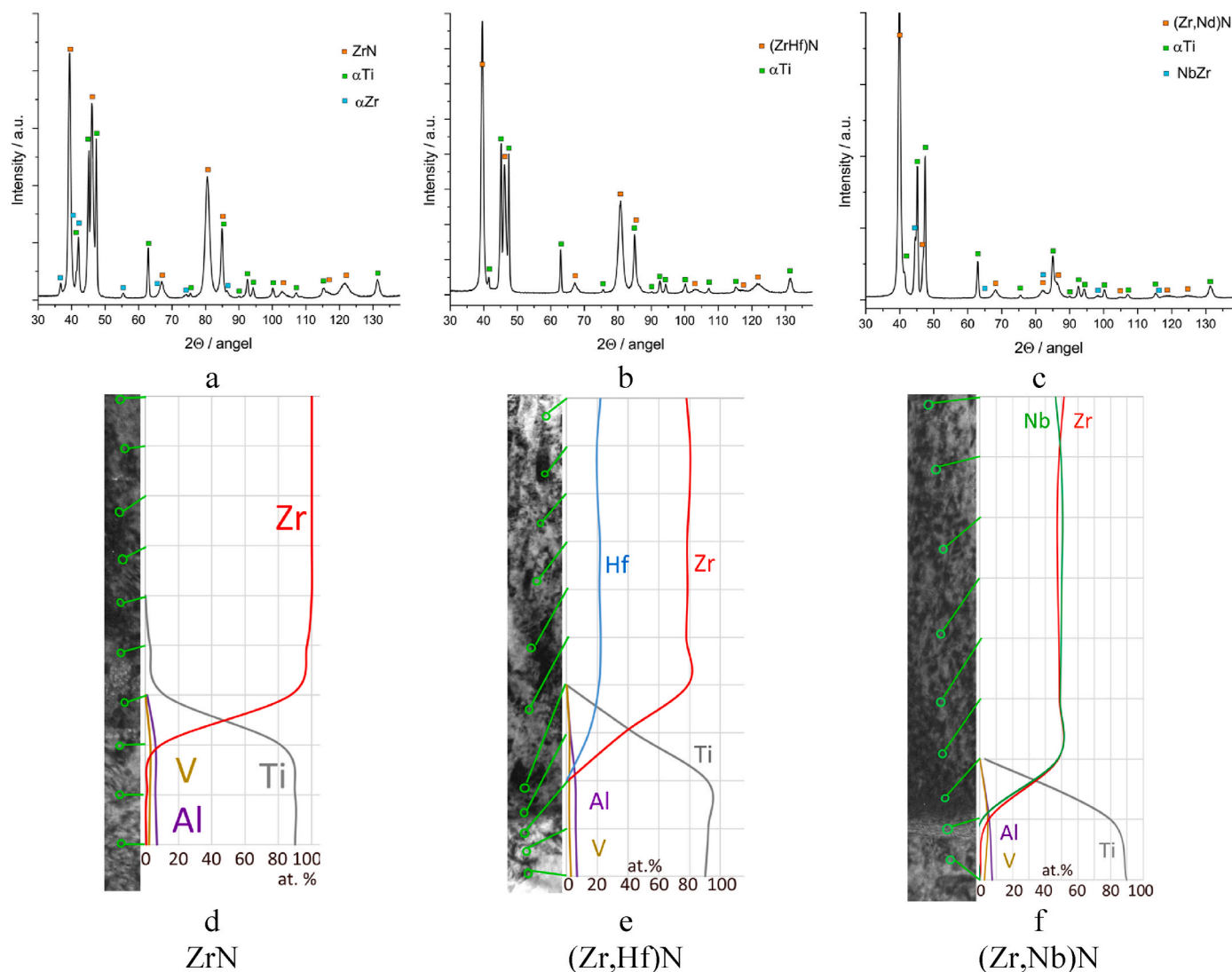
Fig. 3. (a–c) Phase composition of the studied coatings, (d–f) distribution of elements in the coating and the coating-titanium alloy interface (EDX).

Table 2
Hardness of the coatings.

Coating	Hardness, HV
ZrN	2993 ± 85
(Zr,Hf)N	3225 ± 73
(Zr,Nb)N	2436 ± 107

Hank's solution [6,32]. Furthermore, ZrN coatings can significantly improve the corrosion resistance of magnesium alloys [42], 304SS [28], and 304L stainless steel [43] in various media. ZrN coatings are generally hydrophobic owing to the low electronegativity of Zr [22]. Corrosion of the ZrN coating occurs by diffusion of an electrolyte through the pores and cracks of the coating and its contact with the substrate material [44]. It has been established that zirconium oxynitrides (ZrNO) have poorer corrosion resistance compared with ZrN, and ZrN coatings can have biocidal properties against S. aureus bacteria [38].

When heated in air, partial decomposition of the nitride phase and the formation of oxides and oxynitrides (ZrN_xO_y and ZrO_2) are observed on the surface of the ZrN coating, which increases the resistance to pitting corrosion [21]. The ZrN coating noticeably improves the corrosion resistance of samples in Na_2SO_4 aqueous solution [45]. When applying a ZrN coating, a significant increase (by a factor of 122) in the resistance to charge transfer during corrosion in a salt medium is observed [46]. ZrN coatings also have the highest corrosion resistance in anion-based ionic liquids compared with uncoated samples and samples with TiN or CrN coatings [47]. A two-layer ZrN/Zr coating has been used to protect magnesium alloy AZ91 from corrosion [48]. The uncoated corrosion potential of AZ91 alloy is −1830 mV in the SBF environment, and the potential shifts to −1420 mV when the alloy is coated with ZrN/Zr.

Notably, the electrochemical impedance spectroscopy (EIS) spectrum of uncoated AZ91 alloy is characterized by three well-defined loops: a capacitive loop at high frequencies, a capacitive loop at mid frequencies, and an inductive loop at low frequencies. The EIS spectrum of the AZ91 alloy coated with Zr–ZrN in SBF contains two loops: capacitive at high frequencies and capacitive at low frequencies. The capacitive loop in the high-frequency mode is the result of charge transfer and film effects in corrosion; the capacitive loop at the medium frequency is associated with mass transfer processes in the solid phase, and the inductive loop is associated with dissolution processes [48]. The values of the charge transfer resistance R2 (1432 Ω × cm²) and the resistance of the layer of corrosion products R1 (242 Ω × cm²) for the AZ91 alloy with a Zr–ZrN coating are almost an order of magnitude higher than those for the uncoated sample, indicating an increased corrosion resistance for the coated sample in SBF [48].

Titanium alloy samples, Ti6Al–4V, have been characterized by the

a

b   c   d
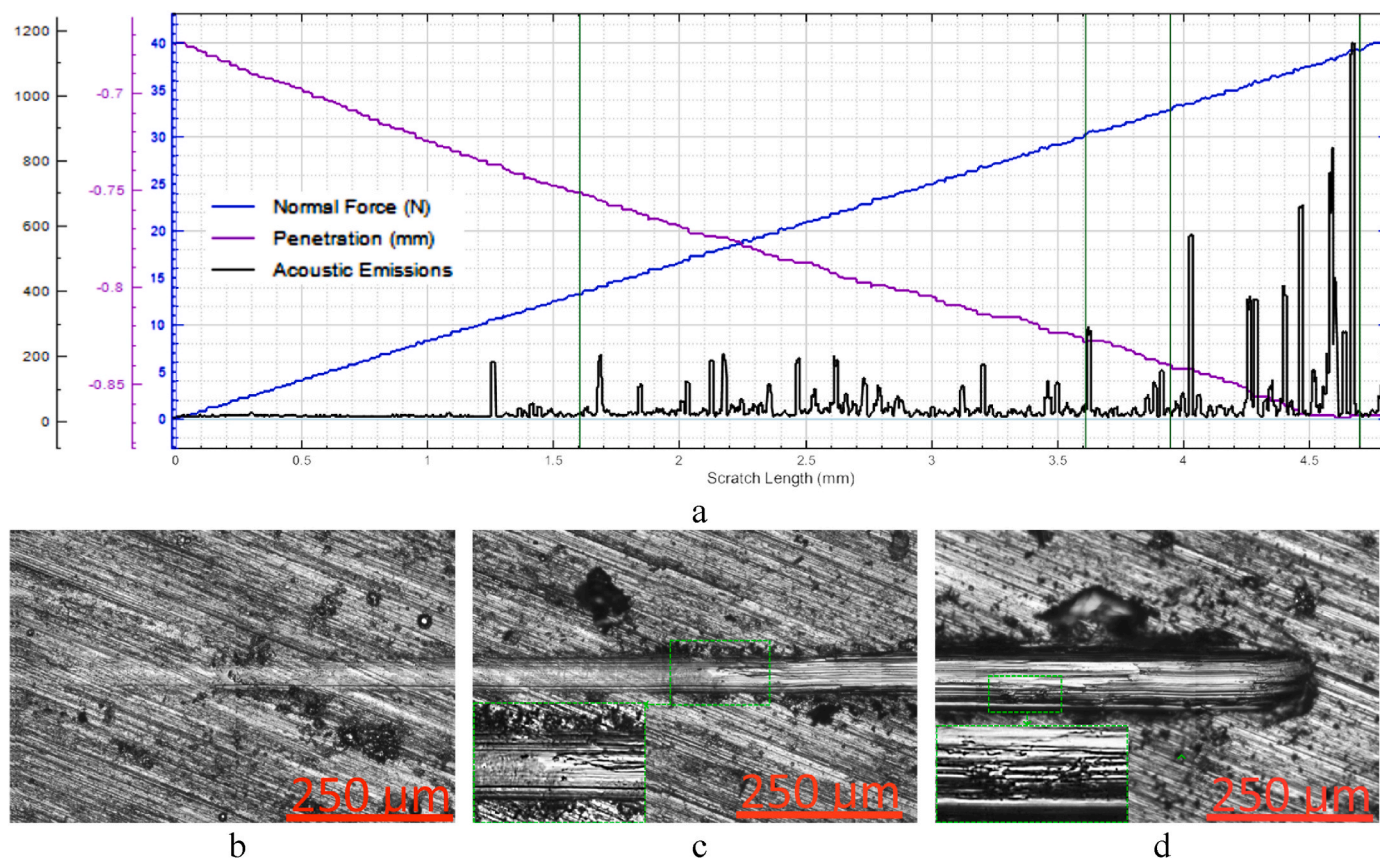
Fig. 4. Study of the strength of the ZrN coating during the scratch test. (a) Acoustic emission diagram, (b) start of furrow formation, (c) start of coating failure, and (d) complete failure of the coating.

process of self-passivation in 0.9 % isotonic NaCl solution, which determines the presence of a passivation area in the potential range of −0.40 to +0.65 V [49]. The gap of the passivating film occurs in the region of transpassivation with an increase in the anode potential, and the current density sharply increases as the corrosion proceeds. Additionally, the EIS spectrum of the Ti6Al–4V alloy with a ZrN coating is characterized by a loop of a larger diameter, which corresponds to high corrosion resistance.

The corrosion properties of the NbN coating have also been studied. When NbN is deposited on a magnesium alloy, WE43, the corrosion potential shifts in the positive direction (from −1.991 V to −1.805 V) in SBF [50]. The uncoated WE43 alloy has a corrosion current density of 5.593×10^{-4} A cm^{-2} in SBF, whereas the NbN-coated sample has a value of 3.817×10^{-5} A cm^{-2}. On the Nyquist plots for the WE43 alloy, both with and without NbN coating, there are two capacitive loops [50]. In addition, the capacitive loops for the NbN-coated sample are larger than those for the uncoated sample, indicating a higher corrosion resistance for the NbN-coated sample in SBF.

For an equivalent circuit of two series-connected Voigt elements with resistances of R1 and R2, the resistance between the working electrode and the reference electrode, Rs, for an uncoated sample and a sample with an NbN coating is 17.3 and 16.3 $\Omega \times$ cm^2, respectively [50]. The resistance to the ion current flowing through the pores (R1) for the uncoated sample is 50.2 Ω cm^2, and that for the sample coated with NbN is 926.0 $\Omega \times$ cm^2. The element R2 represents the charge transfer resistance (i.e., the resistance to the dissolution of the substrate metal). The resistance value R2, which represents the charge transfer resistance, is 9.0 $\Omega \times$ cm^2 for the uncoated sample and 1116 $\Omega \times$ cm^2 for the NbN-coated sample [50].

During the oxidation of the (Zr,Nb)N coating, it is possible to form a two-layer film consisting of an outer layer based on monoclinic ZrO$_2$ and

an inner layer based on tetragonal ZrO$_2$ [11]. The addition of just a small amount of Nb (1.3 at%) makes it possible to improve the oxidation resistance, but with an increase in the Nb content, the oxidation resistance may decrease [11].

The introduction of Hf into the composition of the ZrN coating also makes it possible to noticeably increase the resistance to oxidation [7,9]. The oxidation resistance of the coating increases with the introduction of Hf, which has been attributed to a reduction in the diffusion paths for oxygen ions and an increase in stoichiometry, combined with the high thermal stability of HfN [51]. Moreover, the introduction of a larger amount (21 %) of Hf leads to a deterioration in the oxidative resistance of the coating [52]. During the oxidation of the (Zr,Hf)N coating, the formation of a mixed oxide layer consisting of ZrO$_2$ and HfO$_2$ has been observed [52].

The major conclusions from the literature can be summarized as follows:

- Coatings based on the ZrN system demonstrate high performance in terms of mechanical properties and are considered an alternative to widely used coatings based on the TiN system.
- An additional advantage of ZrN coatings is their anticorrosion properties.
- Improving the characteristics of coatings based on the ZrN system can be achieved by introducing Hf and Nb into their composition.

Thus, studies were carried out on the properties of (Zr,Nb)N, (Zr,Hf)N, and ZrN coatings. However, no direct comparison of the properties of these coatings has been made. Such a comparison can be useful for studying the influence of Nb and Hf, as well as for the convenience of choosing the composition of coatings for corrosion protection.

In this work, the mechanical properties (hardness, wear resistance,
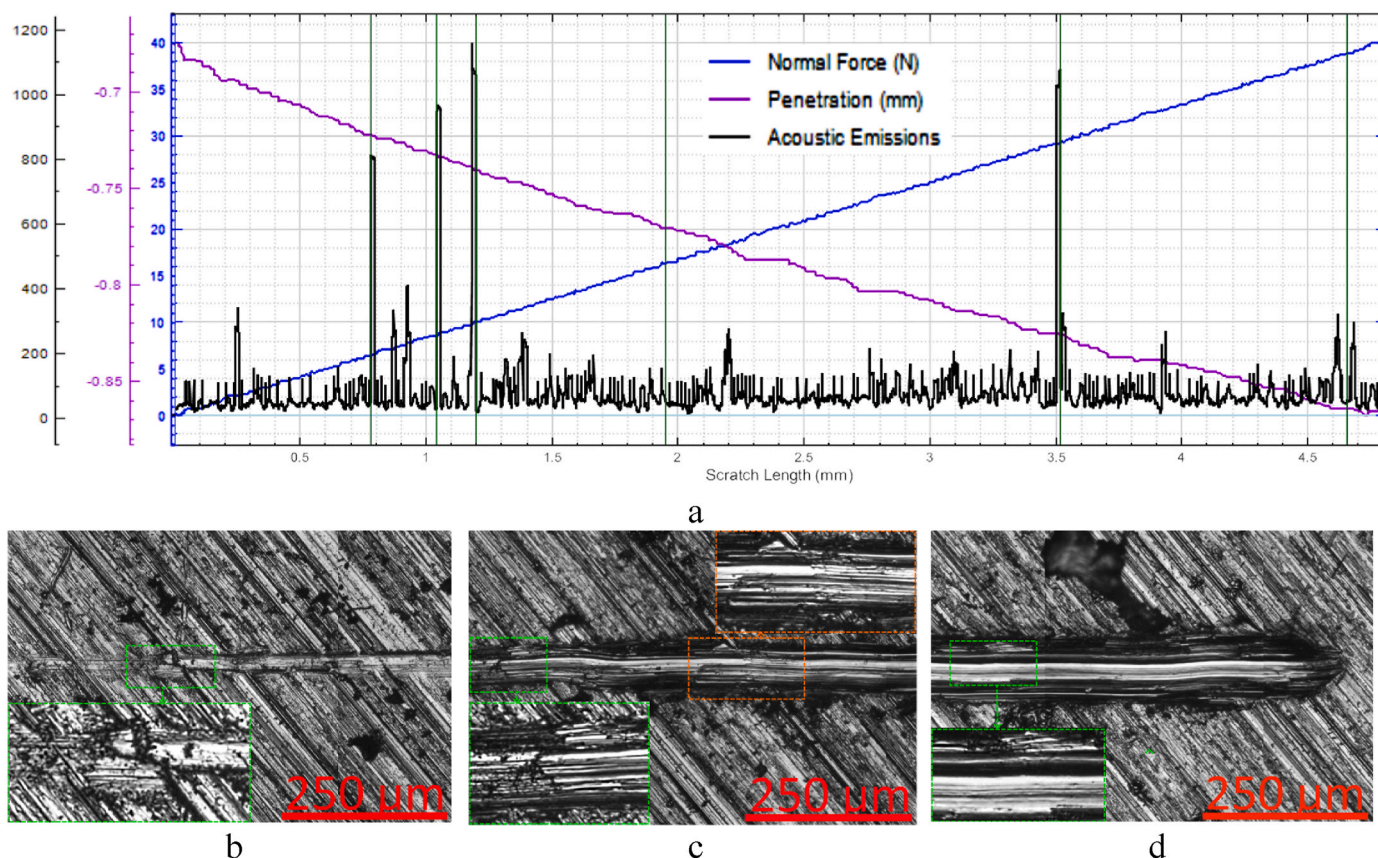
Fig. 5. Study of the strength of the (Zr,Nb)N coating during the scratch test. (a) Acoustic emission diagram, (b) start of furrow formation, (c) start of coating failure, and (d) complete failure of the coating.

and scratch strength) and corrosion resistance of (Zr,Nb)N and (Zr,Hf)N coatings are examined and compared with those of ZrN.

2. Materials and methods

2.1. Coating deposition technique

For the deposition of coatings, titanium alloy samples (Ti6Al–4V [53]) were used (see Table 1). This alloy is widely used in practical applications, particularly in the manufacturing of medical implants.

Cylindrical samples were used (Ø 24 × 2) with a hole (Ø 2) for fixing the sample in the installation chamber (Fig. 1a).

Coatings were deposited in a dedicated physical vapor deposition (PVD) facility (IDTI RAS – MSTU STANKIN, Russia) [54–57], using a controlled accelerated arc-PVD system [58–60].

Before the coating deposition, samples were first washed in a solvent with ultrasonic stimulation, and then in a stream of purified water. Then, the samples were dried in a stream of purified air and mounted on a tool (Fig. 1b).

Preliminary ion etching was carried out in an argon atmosphere at a gas pressure of 0.20 Pa and an arc current of 100–150 A (Fig. 1c). Then the coating was deposited within 90 min (Fig. 1d) using the following parameters:

- chamber gas, pressure: N_2, 0.42 Pa
- substrate voltage: −150 V
- arc current: 65 A (for 99.98 Zr cathode), 65 A (for 50/50 Zr–Nb cathode), 75 A (for 50/50 Zr–Hf cathode)

2.2. Study of the structure and mechanical properties of coatings

For nanostructural studies, a JEM 2100 transmission electron microscope (TEM) (JEOL, Tokyo, Japan) was used at an accelerating voltage of 200 kV. The structures and compositions of the coatings were examined using a TEM with an energy-dispersive X-ray system (EDX) INCA (OXFORD Instruments, Oxford, UK).

Hardness was measured using a Nanovea SV-500 tester (Nanovea, Irvine, CA, USA) with a Berkovich pyramidal indenter at a load of 20 mN. Hardness was determined as the average value of 40 measurements.

The standard ASTM method "Standard Test Method for Wear Testing with a Pin-on-Disk Apparatus" [61] was used to study the wear resistance. This test method is a laboratory procedure for determining sliding wear of materials using a pin-on-disk apparatus. Materials are tested in pairs under nominally non-abrasive conditions. A stationary pin is pressed against a rotating disk under a given load. This wear test method uses two specimens. One, a pin with a rounded tip, is positioned perpendicular to the other, which is a disk with a flat surface (see Fig. 1a). The testing machine causes the disk to rotate around the center. Thus, the sliding trajectory of the pin is a circle on the surface of the disk. The plane of the disk in this case is oriented horizontally. The pin is pressed against the disk with a given load. The results of wear are expressed as the loss of disk volume in cubic millimeters. This method and this equipment were also used to measure the coefficient of friction.

The studies were carried out under the following parameters: D6 Al_2O_3 spherical indenter, load of 10 N, rotation speed of 100 rpm, and measurement duration of 4000 s.

The ASTM "Standard Test Method for Adhesion Strength and Mechanical Failure Modes of Ceramic Coatings by Quantitative Single Point Scratch Testing" [62] was used to study the scratch test failure pattern and the adhesive bond strength with the substrate. In this test method, a
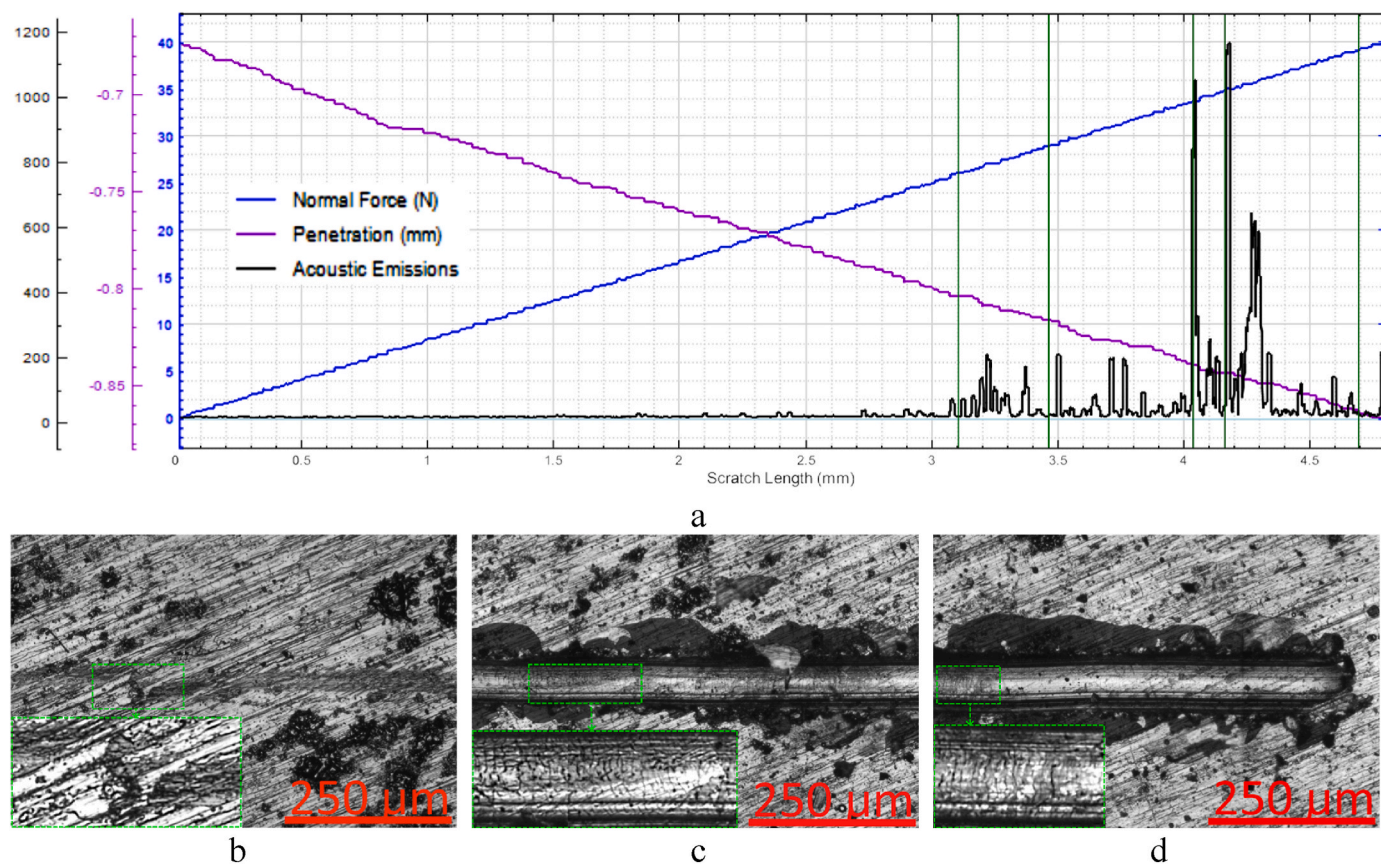
Fig. 6. Study of the strength of the (Zr,Hf)N coating during the scratch test. (a) Acoustic emission diagram, (b) start of furrow formation, (c) start of coating failure, and (d) complete failure of the coating.

diamond stylus of a defined geometry (Rockwell C, 120° conical diamond indenter with 100 μm spherical tip radius) slides along the flat surface of a coated test piece at a constant speed and a progressively increasing normal force over a specified distance. Damage along the scratch is assessed using microscopy and acoustic emission data depending on the force applied. Certain levels of progressive damage are associated with increases in normal strength. The force levels that cause a certain level of damage to the coating are defined as the critical scratch load.

The studies were performed using a Nanovea scratch tester (Nanovea, Irvine, CA, USA) with a load linearly increasing from 0.05 to 40 N. The length of the scratches was 4.8 mm. Three tests were carried out on each sample.

2.3. Potentiodynamic polarization measurements and electrochemical impedance spectroscopy

Potentiodynamic polarization (PDP) measurements were conducted to evaluate the corrosion-electrochemical behavior of ZrN, (Zr,Nb)N, and (Zr,Hf)N coatings on Ti6Al–4V in a 3 % NaCl solution. The tests were performed at a potential sweep rate of 1 mV/s and started when the electrode polarization was ±800 mV [3,38,42,48–50,63] from the potential value that has been established for 1 h. PDP was carried out in a YASE-2 three-electrode electrochemical cell with a graphite auxiliary electrode and a saturated silver-chloride reference electrode at an ambient temperature of 25 °C using an Autolab PGSTAT302 N instrument (Metrohm, Herisau, Switzerland). The area of the region under study was 1 cm². Potential values are presented on the hydrogen scale.

The parameters of the corrosion process in a 3 % NaCl solution were calculated using the Nova 2.0 software by determining the polarization resistance at low polarizations ($\eta = \pm 40$ mV):

$$\eta \approx \frac{RT}{nF} \frac{i}{i_0} = R_0 i \tag{1}$$

where $R_0 = \frac{RT}{i_0 nF}$ represents the charge transfer resistance, measured in Ohms (Ω) [3].

EIS was performed to assess the transient resistance to the electrochemical corrosion process, which makes it possible to obtain a quantitative and qualitative description of the main factors that determine the kinetics of the electrochemical process without damaging or changing the characteristics of the sample surface.

EIS studies of the corrosion behavior for ZrN, (Zr,Nb)N, and (Zr,Hf)N coatings on Ti6Al–4V were carried out in 3 % NaCl solutions using an Autolab PGSTAT302 N instrument (Metrohm, Herisau, Switzerland) equipped with an FRA 32 N impedance spectroscopy module. EIS spectra were taken at the potential value that was established 1 h after the samples were immersed in the test solution. The measurement frequency range was 10^6–10^{-2} Hz, with an oscillation amplitude of 10 mV and 10 points per decade of oscillations. The analyses of EIS spectra, the selection of equivalent circuits, and their calculations were carried out using the Nova 2.0 program.

3. Results

3.1. Hardness, structure, and composition

The coatings under study have almost identical thicknesses (3.2–3.4 μm). Since the coatings were deposited while the substrate was rotated in the chamber, a layered structure formed with a sublayer thickness of 0.6–0.7 μm (Fig. 2a–c). The interfaces between the coatings and the titanium alloy substrate are quite complex (Fig. 2 d-f). Since coating
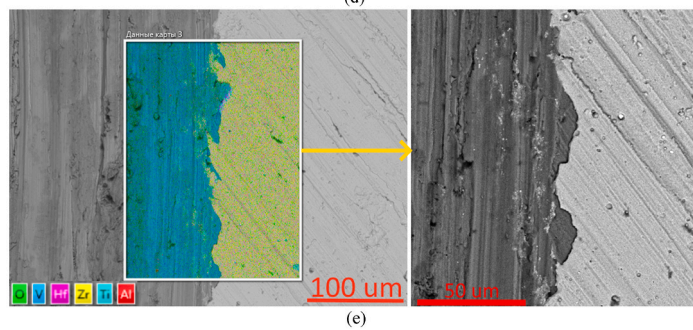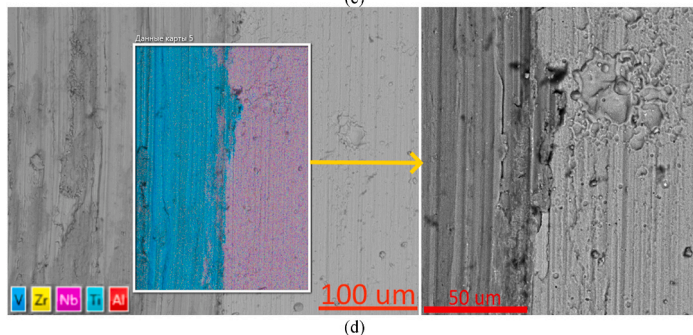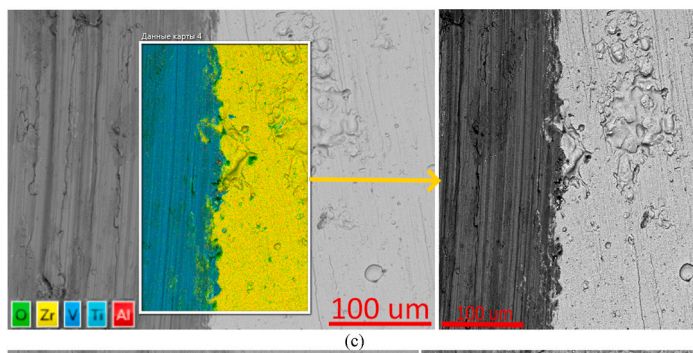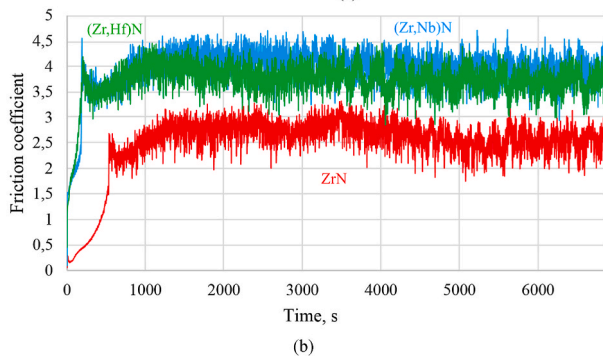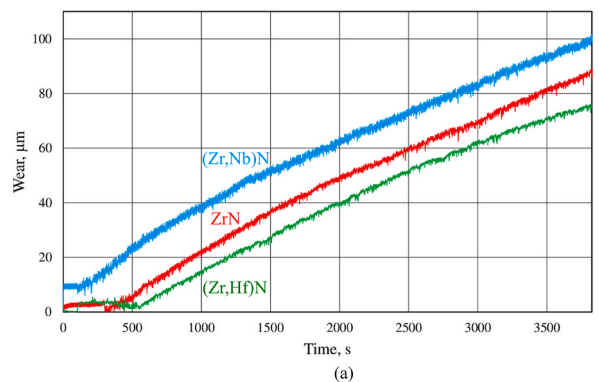
Fig. 7. The results of (a) friction coefficient tests and (b) wear resistance and (c–e) the nature of destruction in the pin-on-disc test and maps of elements distribution on wear boundaries for samples coated with (c) ZrN, (d) (Zr,Nb)N and (e) (Zr,Hf)N.
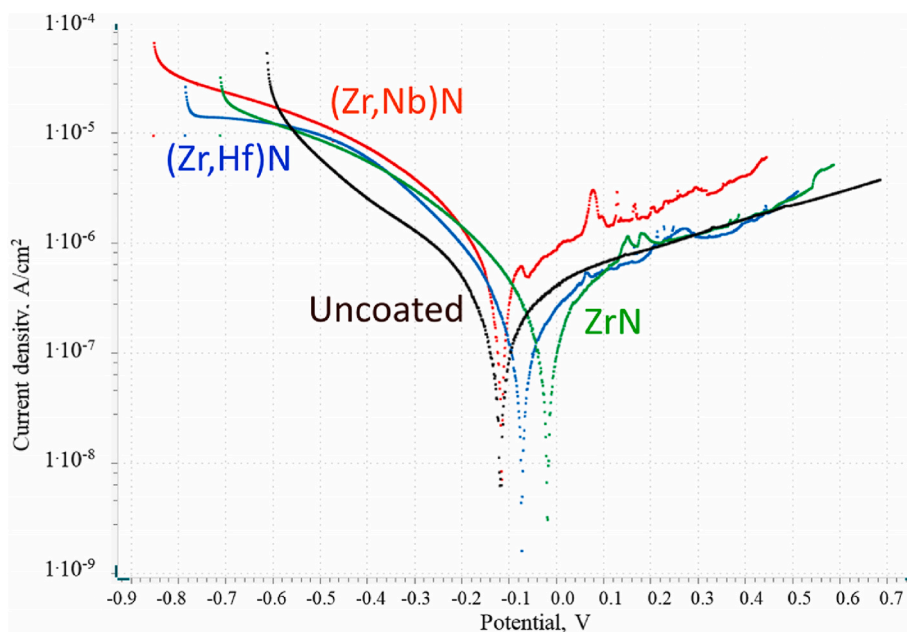
Fig. 8. The potentiodynamic curves of the uncoated samples and samples with ZrN, (Zr,Nb)N, and (Zr,Hf)N coatings in 3 % NaCl (potential sweep rate, Vp = 1 mV/s).

Table 3

Analysis of the corrosion process for uncoated samples and samples with ZrN, (Zr,Nb)N, and (Zr,Hf)N coatings in a 3 % NaCl aqueous solution at 25 °C by determining the polarization resistance in Nova 2.0.

	Coating	E_{cor}, V	Polarization resistance method		
			i_{cor}, $\mu A/cm^2$	D, $\mu m/year$	R0, $k\Omega \times cm^2$
1	(Zr, Nb) N	−0.114	0.395	3.44	66.0
2	(Zr, Hf) N	−0.073	0.118	0.98	232.8
3	ZrN	−0.017	0.127	1.11	204.6
4	uncoated	−0.117	0.128	1.12	203.3

deposition is preceded by ion etching and thermal activation of the substrate surface, and then a thin (several tens of nanometers) metal adhesion layer (Zr, Zr, Hf or Zr,Nb) is deposited, then at the boundary of the substrate and the adhesion layer, the formation of alloys from microtals of the substrate and this layer. Thus, instead of a clear boundary between the coating and the substrate, a blurred mixing zone is formed, which is clearly seen in the example of the (Zr,Nb)N coating.

Comparison of the surface morphology of the coated samples (Fig. 2 g-i) shows the practical identity of the surface of the ZrN and (Zr,Hf)N coatings. In this case, the surface of the (Zr,Nb)N coating has a large relief. The amount of microparticle phase in this coating is slightly higher compared to ZrN and (Zr,Hf)N coatings.

The contents in the (Zr,Hf)N coating are 22 at% Hf and 78 at% Zr (average deviation of ±1.1 at%), and in the (Zr,Nb)N coating, the contents are 50 at% Zr and 50 at% Nb (average deviation of ±1.3 at%). Although Zr–Hf and Zr–Nb cathodes with a ratio of 50/50 at% were used, the Hf content in the coating turned out to be noticeably lower than that of Zr. In this case, the ratio of Zr and Nb in the coating corresponds to their ratio in the cathode. The structural and compositional analyses of the coatings reveal the presence of the main cubic phases for ZrN, (Zr,Hf)N, and (Zr,Nb)N (Fig. 3). Substrate phases, αTi and TiV, and coating microparticle phases, Zr and NbZr, are also observed.

Analysis of the distribution of elements in the coating and the coating-titanium alloy interface (Fig. 3 d-f) shows the presence of diffusion of coating elements from the substrate and substrate elements (primarily titanium) into the coating.

The coatings differ in hardness (see Table 2). The (Zr,Nb)N coating

has the lowest hardness, and the (Zr,Hf)N coating has the highest hardness. Thus, the introduction of Hf into the composition of the ZrN coating noticeably increases the hardness, which agrees with the data in Refs. [7–9,30,31]. Conversely, the introduction of Nb does not provide an increase in hardness in this case, but a noticeable decrease in hardness is observed.

The atomic radii of Zr (160 p.m.) and Hf (167 p.m.) are quite close, and the atomic radius of Nb (146 p.m.) is noticeably different from them. Thus, one can expect greater distortion of the crystal lattice when Nb is introduced into the ZrN phase than when Hf is introduced. In this case, in the (Zr,Nb)N coating, with an equivalent content of Zr and Nb, an intermetallic phase of Zr, Nb is also formed. The presence of this phase can reduce the hardness of the (Zr,Nb)N coating. In the (Zr,Hf)N coating, complete dissolution of Hf in the ZrN cubic lattice is observed, which provides an increase in hardness, previously described in a number of works [7–9,30,31].

3.2. Scratch test

The results of the scratch test show a noticeable difference in the nature of the destruction among the three coatings. Comparing the acoustic emission data and the results of scribing, we can conclude that the destruction of the ZrN coating begins at a load of approximately 20 N (point L_{C1}, Fig. 4). Complete destruction of the ZrN coating occurs at a load of 38 N (point L_{C2}). The ZrN coating demonstrates the plastic nature of the fracture, without the formation of extensive chips.

Destruction of the (Zr,Nb)N coating starts at a load of only 6 N (point L_{C1}, Fig. 5). Complete destruction of this coating is observed at a load of 29 N (point L_{C2}, Fig. 5). Active chipping is observed along the edges of the scribing groove, which is also confirmed by the corresponding nature of the acoustic emission. In this case, the width of the shearing region is insignificant.

The nature of the destruction of the coating (Zr,Hf)N is significantly different. This coating is characterized by the formation of an extensive chipping area around the scribed groove. The destruction of the coating begins at a load of approximately 26 N (point L_{C1}, Fig. 6). From the acoustic emission, complete destruction of the coating occurs at a load of 35 N; however, observation of the scribed groove shows that some layer of the coating is preserved at a load of up to 40 N. The scribed groove has
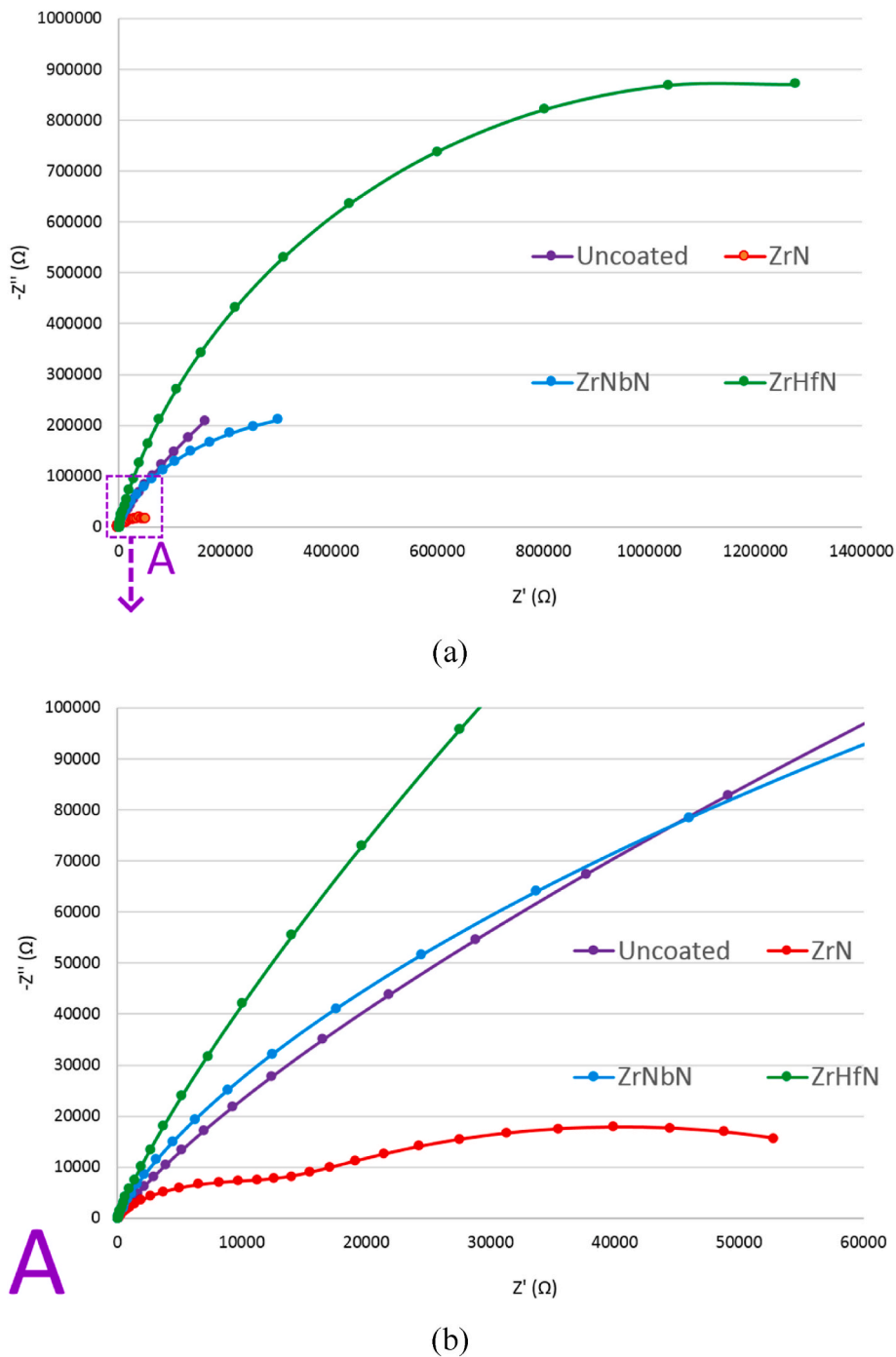
Fig. 9. Electrochemical impedance during the corrosion process for Ti6AL-4V samples without coating and coated with ZrN, (Zr,Nb)N, and (Zr,Hf)N in 3 % NaCl. (a) General view of the graph, (b) enlarged area for ZrN coating.

a network of small transverse cracks, which is not typical for ZrN or (Zr, Nb)N. Thus, we assume that the destruction of the coating (Zr,Hf)N is largely due to the loss of cohesive bonds between the layers of the coating [64,65] and the mechanisms of brittle fracture.

3.3. Wear resistance

The highest wear resistance is provided by samples coated with (Zr, Hf)N (75 μm wear occurs after 3600 s, Fig. 7a), which is consistent with the high hardness of this coating. Sufficiently high wear resistance was also exhibited by samples coated with ZrN (75 μm wear occurs after 3200 s). The samples coated with (Zr,Nb)N have the lowest wear

resistance (75 μm wear occurs after 2600 s), which also agrees well with the relatively low hardness of this coating. Overall, the results of wear resistance correlate well with the scratch test data.

Studies of the friction coefficient (COF) have shown that the ZrN coating provides better tribological conditions (COF = 2.50 … 2.75), coatings (Zr,Hf)N, and (Zr,Nb)N have almost identical COF values (3.50 … 4.00) (Fig. 7b). The coatings have high hardness (hardness was measured at extremely low loads of 20 mN to exclude the influence of a soft substrate). However, when measuring the friction coefficient, surface roughness also influences (in particular, the (Zr,Nb)N coating has a more pronounced relief and, accordingly, a higher friction coefficient) and substrate deformation. That is, when measuring the coefficient of
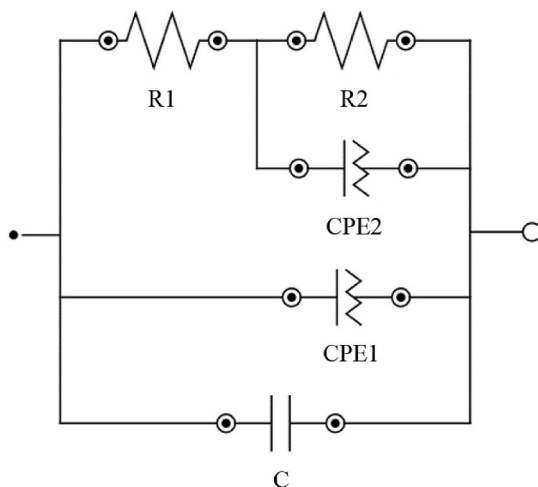
Fig. 10. Equivalent scheme for modeling the EIS spectrum of the Ti6AL-4V sample without coating and with the (Zr,Nb)N coating in 3 % NaCl [38].

friction, the properties of the composite "sufficiently soft substrate - hard coating" are studied. Obviously, similar coatings on a harder substrate (silicon or carbide) will provide a lower coefficient of friction.

Let us consider the wear pattern of the studied samples during the pin-on-disk test (Fig. 7 c-e). Extensive areas of delamination from the substrate for the (Zr,Hf)N sample can be seen (Fig. 7e). At the same time, due to its high hardness, this coating also shows high wear resistance. In contrast, the ZrN coating shows no noticeable signs of delamination from the substrate (Fig. 7c). However, due to lower hardness, the wear resistance of this coating is lower than (Zr,Hf)N. The (Zr,Nb)N coating is the least hard and shows noticeable signs of delamination from the

substrate. Thus, the wear resistance of the (Zr,Nb)N coating is the lowest of the compared samples. Since the adhesive sublayer has a key influence on the strength of the adhesive bond between the coating and the substrate, it can be concluded that the Zr, Hf sublayer provides less of a bond between the coating and the substrate compared to the Zr and Zr, Nb sublayers. Possessing high hardness and wear resistance, the (Zr,Hf)N coating is destroyed due to detachment from the substrate. Thus, the introduction of a sublayer that provides better adhesion to the substrate can significantly improve the performance properties of this coating.

3.4. Corrosion resistance

The results of corrosion resistance tests for Ti6Al–4V samples without coating and with ZrN, (Zr,Nb)N and (Zr,Hf)N coatings in 3 % NaCl are shown in Fig. 8 and Table 3.

The steady-state potential of the corrosion process for Ti6Al–4V is -0.117 V, and the corrosion current density determined by PDP is 0.128 $\mu A/cm^2$, which indicates a high resistance to corrosion in a 3 % NaCl solution. The resistance may be due to the formation of a titanium dioxide dielectric film sample with a charge transfer resistance of 203.3 $k\Omega \times cm^2$, which agrees well with previous studies [66,67]. The polarization curve for the ZrN coating is characterized by a corrosion potential of -0.017 V and a calculated resistance to charge transfer of 204.6 $k\Omega \times cm^2$, which indicates surface passivation and is consistent with the data in Ref. [38]. The similarity of the corrosion current values for the ZrN coating and the uncoated sample can be explained by the formation of a layer consisting of Zr oxides and oxynitrides, which suppresses the process of corrosion dissolution [21,45–47].

The introduction of Hf into the ZrN coating leads to the formation of the (Zr,Hf)N solid solution, reducing the corrosion currents from 0.127 to 0.118 $\mu A/cm^2$, which may be due to the higher chemical stability of HfN compared with ZrN [51]. For samples coated with (Zr,Nb)N, the current density increases by a factor of 3.5 (up to 3.44 $\mu A/cm^2$) because
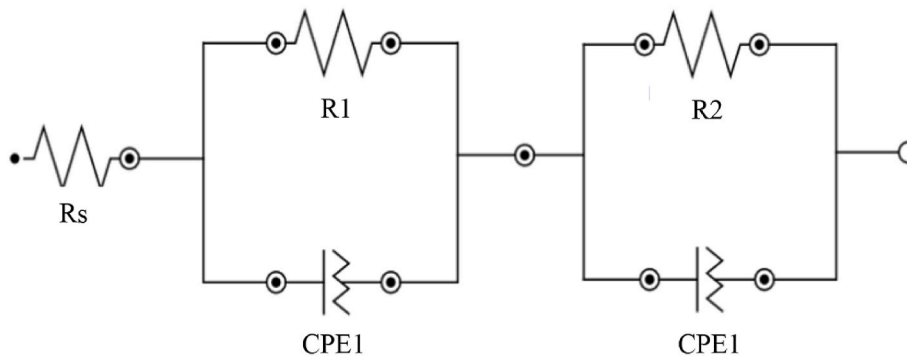
Fig. 11. Equivalent scheme for modeling the EIS spectrum of a Ti6Al–4V sample coated with ZrN in 3 % NaCl [66].
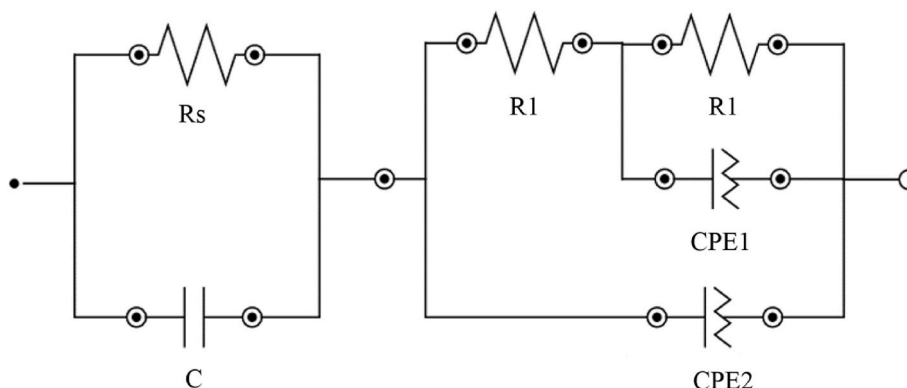
Fig. 12. Equivalent scheme for EIS spectrum analysis of Ti6AL-4V samples coated with (Zr,Hf)N in 3 % NaCl.

Table 4

Calculation results in the Nova 2.0 program of equivalent scheme elements for the analysis of the EIS spectra of Ti6AL-4V samples with and without nitride coatings in a 3 % NaCl medium.

	Coating	Elements of equivalent schemes							
		Rs, $\Omega \times cm^2$	C nF cm^{-2}	CPE1		CPE2		R1, $\Omega \times cm^2$	R2, $M\Omega \times cm^2$
				Y, $\mu S\ s^n\ cm^{-2}$	n	Y, $\mu S\ s^n\ cm^{-2}$	n		
1	(Zr, Nb) N	–	35.7	5.09	0.42	7.42	0.92	38	1.100
2	(Zr, Hf) N	39.8	36.9	0.51	1.10	3.24	0.79	296	2.360
3	ZrN	26.4	–	8.39	0.87	57.81	0.67	10810	0.060
4	uncoated	–	33.7	7.51	0.41	16.17	0.84	38	1100000
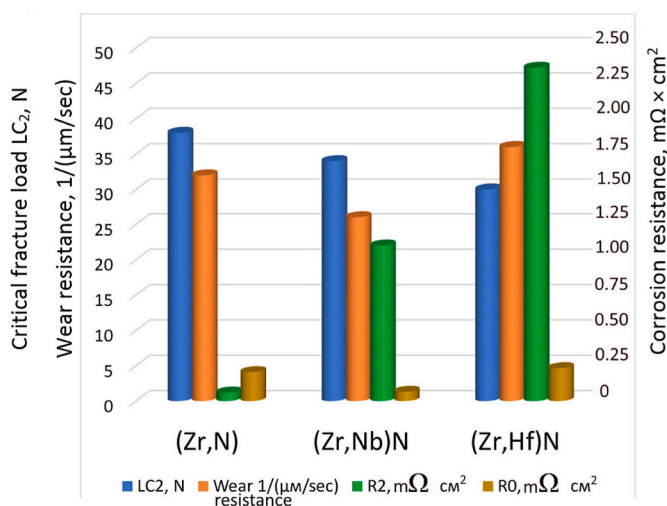
Fig. 13. Comparison of the critical fracture load L_{C2}, wear resistance, defined as the reciprocal of the time required to reach wear of 75 μm (hundreds of seconds) (values on the left scale), and corrosion resistance, defined as resistance to electrochemical corrosion of Ti6AL-4V samples with nitride coatings in 3 % NaCl, determined by EIS (R2) and PDP (R0, × 10) (values on the right scale).

of the oxidative effect of corrosion products containing compounds based on Nb^{+5} [49], ZrN, and the titanium substrate. This effect is described in Ref. [66].

For uncoated samples and samples coated with ZrN, (Zr,Nb)N, and (Zr,Hf)N during corrosion in 3 % NaCl, the electrochemical impedance curves include a high-frequency semicircle, which represents the bulk conductivity in the system, and a suppressed low-frequency semicircle, which describes the blocking effect of the surface conductivity (Fig. 9).

The presence of a large right semicircle on the impedance hodograph (Fig. 9a) for the Ti6AL-4V alloy indicates the predominance of surface conductivity along grain boundaries and pores in the layer of corrosion products.

When analyzing a similar spectrum (Fig. 9b) for a sample coated with ZrN, the left semicircle represents the resistance of the electrolyte, and the right semicircle is the resistance of the grain boundaries. Near the right semicircle of the hodograph, a poorly resolved left semicircle is visible, which represents the bulk conductivity.

4. Discussion

To describe the Nyquist diagram (Fig. 9a, c) of the uncoated sample and the sample with (Zr,Nb)N coating during corrosion in a 3 % NaCl medium, an equivalent circuit is proposed and analyzed using the Nova 2.1 program (Fig. 10a and b), based on a block-layered model. This scheme is described in Ref. [38].

The circuit consists of a Voigt element (with resistance R1 and an element with a constant phase CPE1) connected in parallel with a

capacitance C, which represents the capacitance of the electrolyte-electrode interface. Inside the first Voigt element, in series with the resistance R1, the second Voigt element is connected with the resistance R2 and the constant phase element CPE2. Furthermore, the Rs element (electrolyte resistance) is absent in this circuit because it is much less than the rest of the circuit elements and does not affect the course of the impedance hodograph at the scanned frequencies. The components of the proposed equivalent circuit, R1 and CPE1, similar to Refs. [38,42, 63] (constant phase elements), are responsible for the bulk of the impedance, namely the resistance of the layer of corrosion products and the capacitance of the double layer, respectively. R2 and CPE2 are the charge transfer resistance and capacitance of the dielectric layer of corrosion products, respectively [38,42,63].

Analyzing the numerical values of R1 for electrodes made of Ti6AL-4V without coating and for those with (Zr,Nb)N coating, almost identical resistance values are observed (38.3 and 37.6 $\Omega \times cm^2$, respectively), which is consistent with the previously obtained values of the volume component of the impedance [38,42,63].

The impedance component R2 (charge transfer resistance) for the Ti6AL-4V alloy is 1.1 $T\Omega \times cm^2$, which is associated with the suppression of the corrosion process by the formation of a dense TiO_2 dielectric layer [48] during the primary corrosion of the titanium alloy.

At the same time, when analyzing such a spectrum (Fig. 9c), the impedance of the component R2 for the (Zr,Nb)N coating does not exceed 1.1 $m\Omega \times cm^2$, which is consistent with the data in Ref. [38] and correlates with relatively increased corrosion currents for the coating (Zr,Nb)N calculated from PDP measurements. This behavior of the (Zr,Nb)N coating is attributed to the formation of complex NbO_x oxides [49, 63,66] with increased solubility in water due to acid-base interactions. In this case, the layer of corrosion products may be partially destroyed, enhancing the corrosion process, as described in Ref. [66] for the NbN coating. However, the order of magnitude of charge transfer resistance R2 indicates that low corrosion rates are expected for (Zr,Nb)N-coated Ti6Al–4V specimens in 3 % NaCl.

For the corrosion process of samples coated with ZrN in 3 % NaCl, the equivalent circuit describing the Nyquist diagram is a series connection of the resistance Rs and two Voigt elements (Fig. 11). This scheme is also considered in Ref. [66].

Rs corresponds to the volume resistance of the electrolyte, R1 corresponds to the resistance of the layer of corrosion products, CPE 1 is a constant phase element that describes the charge transfer, and R2 (resistance to charge transfer) and CPE 2 (capacitance of the dielectric layer of corrosion products) are responsible for the totality of processes occurring at the electrode-electrolyte interface. In the impedance hodograph for samples coated with ZrN in 3 % NaCl (Fig. 9b), the left semicircle is characterized by the electrolyte resistance Rs (26.4 $\Omega \times cm^2$). The right semicircle in Fig. 7b is described by the resistance R1 with a value of 10.8 $k\Omega \times cm^2$ and characterizes the resistance of the layer of corrosion products. The charge transfer resistance R2 at the electrolyte-electrode interface is 60.5 $k\Omega \times cm^2$, which indicates the formation of a ZrO_2 dielectric film during corrosion and suppression of the dissolution process, which is also described in Ref. [38].

To describe the impedance spectra of the Ti6AL-4V sample coated with (Zr,Hf)N in 3 % NaCl, an equivalent circuit is proposed (Fig. 12)

based on the block-layered model with Voigt elements and the previously presented scheme (Fig. 10).

The equivalent circuit selected for modeling impedance dependencies is shown in Fig. 12 and consists of a Voigt element (with resistance R1 and an element with a constant phase CPE1), inside which a second Voight element is connected in series with the resistance R1 (with a resistance R2 and an element with a constant phase CPE2). In this circuit, there is an element Rs (electrolyte resistance), similar to the previously considered circuit (Fig. 10). The circuit elements R1 and CPE1, similar to Refs. [38,42,63], are responsible for the resistance of the layer of corrosion products and the capacitance of the double layer, respectively. R2 and CPE2 represent the charge transfer resistance and capacitance of the dielectric layer of corrosion products, respectively. In parallel with the resistance Rs (39.8 $\Omega \times cm^2$), a capacitance C is connected, which denotes the capacitance of the electrolyte-electrode interface.

The observed right semicircle in Fig. 9d for the Nyquist plot of the (Zr,Hf)N-coated sample is most likely associated with the formation of a dense (Zr,Hf)O$_x$ dielectric layer during corrosion [67], which has a resistance R1 of 269.0 $\Omega \times cm^2$. The impedance component R2 for the (Zr,Hf)N coating is 2.36 m$\Omega \times cm^2$, which agrees well with the data in Ref. [42] and corresponds to the high corrosion resistance of the coating observed during polarization studies (Table 4).

Thus, the impedance studies of the corrosion resistance of Ti6AL-4V samples with nitride coatings in 3 % NaCl show that the corrosion process is limited by the charge transfer resistance (R2), which is present in all types of equivalent circuits describing impedance spectra. It should be noted that the maximum value of this resistance (1.1 T$\Omega \times cm^2$) is observed for the uncoated Ti6AL-4V alloy, which self-passivates in a 3 % NaCl medium to form a dense TiO$_2$ film that is several nanometers thick. However, this film is relatively easy to destroy by mechanical and chemical action.

The use of nitride coatings makes it possible to achieve R2 values from 60 to 2360 k$\Omega \times cm^2$, which agrees well with the polarization measurements for these coatings (Table 3, Fig. 13).

In addition, the values of polarization resistance range from 66.0 to 232.8 k$\Omega \times cm^2$ and characterize the corrosion resistance along the coating depth, in contrast to the impedance, which is associated with the surface properties of the nitride coatings.

The maximum R2 value (charge transfer resistance) of 2.36 m$\Omega \times cm^2$, calculated from the equivalent circuit describing the impedance spectra (Fig. 9), is observed for the (Zr,Hf)N coating, which also has the maximum polarization resistance value (232.8 k$\Omega \times cm^2$), which determines the PDP charge transfer in 3 % NaCl.

Thus, according to the results of two electrochemical methods of investigation EIS and PDP, a sample coated with (Zr,Hf)N has the highest resistance to corrosion in 3 % NaCl, which is associated with doping of the ZrN layer using 22 at% Hf during the coating deposition. In this case, the oxidation of this coating proceeds without the formation of a separate phase of Hf oxide or mechanical destruction of the nitride layer in this process, as described in Ref. [52]. The (Zr,Nb)N coating has 50 at% Nb doping, which leads to a 2.5-fold decrease in the resistance to the corrosion process (Fig. 13) compared with the (Zr,Hf)N coating. This may be due to the delamination of the oxide layer covering the (Zr,Nb)N when the corrosion proceeds deep into the sample [49,50,66].

The value of corrosion resistance for the ZrN coating, as determined by EIS, is 12–25 times less than the values for ZrN coatings doped with Nb and Hf, demonstrating the effectiveness of complex systems based on (Zr,Nb)N and (Zr,Hf)N for protection of the Ti6AL-4V alloy against corrosion. The observed phenomenon is most likely due to the shortening of the diffusion paths for oxygen ions in the Zr oxide formed during corrosion, owing to the incorporation of Nb and Hf into the lattice, which is isovalent to Zr [7,8].

Fig. 13 compares the properties of the three coatings. Notably, the (Zr,Hf)N coating has the highest wear resistance and corrosion resistance in 3 % NaCl but is inferior to the other coatings in terms of the adhesion strength with the Ti6Al–4V substrate.

One of the future directions of this work can be to increase the adhesive bond of this coating with the substrate, which may be achieved by changing the composition of the adhesive layer.

5. Conclusions

The properties of coatings based on the ZrN system with the introduction of hafnium and zirconium (ZrN, (Zr,Nb)N and (Zr,Hf)N), deposited on a Ti6Al–4V titanium alloy substrate are compared. A comparison was made of hardness, structure and composition parameters, the strength of the adhesive bond with the substrate in the scratch test, wear resistance and coefficient of friction in the pin-on-disk test, and corrosion resistance in a 3 % NaCl solution. The following results were obtained:

- Coating (Zr,Hf)N (22 % Hf and 78 % Zr) has the maximum hardness (HV, 3225 $\pm$ 73) and wear resistance (wear of 75 μm is achieved after 3600 s of testing).
- It has been established (by PDP) that the introduction of Hf into ZrN makes it possible to suppress the corrosion process in 3 % NaCl to a rate of 0.118 μA/cm^2, whereas the addition of Nb to the ZrN system accelerates corrosion by 3.5 times (3.440 μA/cm^2).
- It has been established (by EIS) that for uncoated Ti6Al–4V and samples coated with ZrN, (Zr,Nb)N, and (Zr,Hf)N and corroded in 3 % NaCl, the electrochemical impedance includes a high-frequency semicircle, and the corrosion process is determined by charge transfer resistance (R2) present in all types of equivalent circuits describing EIS spectra. The (Zr,Hf)N coating has the highest charge transfer resistance (2.36 m$\Omega \times cm^2$), which is consistent with the maximum value of the polarization resistance (232.8 k$\Omega \times cm^2$) determined by PDP.
- The value of charge transfer resistance for ZrN coating, determined by EIS, is 12–25 times less than the corresponding resistance for Nb-doped (50 %) and Hf-doped (20 %) ZrN coatings, which indicates the effectiveness of complex systems based on (Zr,Nb)N and (Zr,Hf)N for the protection of Ti6Al–4V against corrosion in 3 % NaCl.
- The (Zr,Hf)N coating has the highest wear and corrosion resistance in 3 % NaCl. Thus, this coating can be recommended for increasing the wear resistance of friction pairs operating in NaCl aqueous solutions (for example, in seawater).

Statements & declarations

Conflicts of interest/competing interests

The authors have no relevant financial or non-financial interests to disclose.

Author Contributions

All authors contributed to the study conception and design. Material preparation, data collection and analysis were performed by He Tao, Valery Zhylinski, Alexey Vereschaka, Anthon Keshin, Huo Yuanming, Filipp Milovich, Catherine Sotova, Anton Seleznev. The first draft of the manuscript was written by Alexey Vereschaka, Valery Zhylinski and He Tao and all authors commented on previous versions of the manuscript. All authors read and approved the final manuscript.

Declaration of competing interest

The authors declare that they have no known competing financial interests or personal relationships that could have appeared to influence the work reported in this paper.

References

[1] Jianxin D, Jianhua L, Jinlong Z, Wenlong S, Ming N. Friction and wear behaviors of the PVD ZrN coated carbide in sliding wear tests and in machining processes. Wear 2008;264(3–4):298–307.

[2] Zhitomirsky VN, Grimberg I, Boxman RL, Travitzky NA, Goldsmith S, Weiss BZ. Vacuum arc deposition and microstructure of ZrN-based coatings. Surf Coating Technol 1997;94–95:207–12.

[3] Tao H, Zhylinski V, Vereschaka A, Chayeuski V, Yuanming H, Milovich F, et al. Comparison of the mechanical properties and corrosion resistance of the Cr-CrN, Ti-TiN, Zr-ZrN, and Mo-Mon coatings. Coatings 2023;13(4):750.

[4] Vereschaka A, Tabakov V, Grigoriev S, Aksenenko A, Sitnikov N, Oganyan G, et al. Effect of adhesion and the wear-resistant layer thickness ratio on mechanical and performance properties of ZrN-(Zr,Al,Si)N coatings. Surf Coat Technol 2019;357: 218–34.

[5] Grigoriev S, Vereschaka A, Milovich F, Tabakov V, Sitnikov N, Andreev N, et al. Investigation of multicomponent nanolayer coatings based on nitrides of Cr, Mo, Zr, Nb, and Al. Surf Coat Technol 2020;401:126258.

[6] Azibi M, Saoula N, Madaoui N, Aknouche H. Effects of nitrogen content on the structural, mechanical, and corrosion properties of ZrN thin films grown on AISI 316L by radiofrequency magnetron sputtering. Cryst Res Technol 2021;56(12): 2100096.

[7] Fernandez DAR, Brito BSS, Santos IAD, Soares VFD, Terto AR, de Oliveira GB, et al. Effect of hafnium contaminant present in zirconium targets on sputter deposited ZrN thin films. Nucl Instrum Methods Phys Res, Sect B 2020;462:90–4.

[8] Atar E, Sarioglu C, Cimenoglu H, Kayali ES. Residual stresses in (Zr,Hf)N films (up to 11.9 at.% Hf) measured by X-ray diffraction using experimentally calculated XECs. Surf Coating Technol 2005;191(2–3):188–94.

[9] Atar E, Kayali ES, Cimenoglu H. Sliding wear behaviour of ZrN and (Zr, 12 wt% Hf) N coatings. Tribol Int 2006;39(4):297–302.

[10] Krysina OV, Shugurov VV, Prokopenko NA, Petrikova EA, Tolkachev OS, Denisova YA. Cathodic Arc deposition of ZrNbN coating. Russ Phys J 2019;62(6): 956–61.

[11] Wu ZT, Qi ZB, Jiang WF, Wang ZC, Liu B. Influence of niobium addition on microstructure, mechanical properties and oxidation resistance of ZrN coatings. Thin Solid Films 2014;570(PB):256–61.

[12] Kanoun MB, Goumri-Said S. Effect of alloying on elastic properties of ZrN based transition metal nitride alloys. Surf Coating Technol 2014;255:140–5.

[13] Kakanakov R, Bahchedjiev Hr, Kolaklieva L, Cholakova T, Evtimova Sv, Polyhroniadis E, et al. Investigation of ZrN hard coatings obtained by cathodic arc evaporation. Solid State Phenom 2010;159:113–6.

[14] Arias DF, Arango YC, Devia A. Study of TiN and ZrN thin films grown by cathodic arc technique. Appl Surf Sci 2006;253(4):1683–90.

[15] Yu S, Zeng Q, Oganov AR, Frapper G, Huang BH, Niu LZ. First-principles study of Zr–N crystalline phases: phase stability, electronic and mechanical properties. RSC Adv 2017;7:4697–703.

[16] Yin L-C, Saito R. First principles calculations of the electronic structure of ZrN allotropes. J Phys Soc Jpn 2011;80:114707.

[17] Kuznetsova T, Lapitskaya V, Warcholinski B, Gilewicz A, Chizhik S. Friction and wear of ZrN coatings under conditions of microcontact using atomic-force microscopy. J Frict Wear 2020;41(4):287–94.

[18] Kuznetsova T, Lapitskaya V, Khabarava A, Chizhik S, Warcholinski B, Gilewicz A. The influence of nitrogen on the morphology of ZrN coatings deposited by magnetron sputtering. Appl Surf Sci 2020;522:146508.

[19] Singh A, Kuppusami P, Khan S, Sudha C, Thirumurugesan R, Ramaseshan R, et al. Influence of nitrogen flow rate on microstructural and nanomechanical properties of Zr-N thin films prepared by pulsed DC magnetron sputtering. Appl Surf Sci 2013; 280:117–23.

[20] Saleh AS. Study of deposition temperature effect on defect density in ZrN thin films by positron annihilation. Procedia Eng 2014;75:34–8.

[21] Roman D, Bernardi J, Amorim CLGD, De Souza FS, Spinelli A, Giacomelli C, et al. Effect of deposition temperature on microstructure and corrosion resistance of ZrN thin films deposited by DC reactive magnetron sputtering. Mater Chem Phys 2011; 130(1–2):147–53.

[22] Musil J, Zenkin S, Kos Š, Čerstvý R, Haviar S. Flexible hydrophobic ZrN nitride films. Vacuum 2016;131:34–8.

[23] Huang J-H, Chen Y-H, Wang A-N, Yu G-P, Chen H. Evaluation of fracture toughness of ZrN hard coatings by internal energy induced cracking method. Surf Coating Technol 2014;258:211–8.

[24] Zhu F, Zhu K, Hu Y, Ling Y, Wang D, Peng H, et al. Microstructure and Young's modulus of ZrN thin film prepared by dual ion beam sputtering deposition. Surf Coating Technol 2019;374:997–1005.

[25] Grigoriev S, Vereschaka A, Uglov V, Milovich F, Cherenda N, Andreev N, et al. Influence of tribological properties of Zr-ZrN-(Zr,Cr,Al)N and Zr-ZrN-(Zr,Mo,Al)N multilayer nanostructured coatings on the cutting properties of coated tools during dry turning of Inconel 718 alloy. Wear 2023;512–3. 204521.

[26] Grigoriev S, Vereschaka A, Milovich F, Tabakov V, Sitnikov N, Andreev N, et al. Investigation of the properties of Ti-TiN-(Ti,Al,Nb,Zr)N composite coating and its

[27] Vereschaka A, Milovich F, Migranov M, Andreev N, Alexandrov I, Muranov A, et al. Inves-tigation of the tribological and operational properties of (Mex,Moy,Al1-(x+y))N (Me–Ti, Zr or Cr) coatings. Tribol Int 2022;165:107305.

[28] Huang J-H, Kuo K-L, Yu G-P. Oxidation behavior and corrosion resistance of vacuum annealed ZrN-coated stainless steel. Surf Coating Technol 2019;358: 308–19.

[29] Huang J-H, Ting I-S, Zheng T-W. Evaluation of stress and energy relief efficiency of ZrN/Ti and ZrN/Zr. Surf Coating Technol 2022;434:128224.

[30] Atar E, Çimenoğlu H, Kayali ES. Fretting wear of ZrN and Zr(21% Hf)N coatings. Key Eng Mater 2004;264–268(I):477–80.

[31] Atar E, Kayali ES, Cimenoglu H. Reciprocating wear behaviour of (Zr, Hf)N coatings. Wear 2004;257(5–6):633–9.

[32] Ul-Hamid A. Microstructure, properties and applications of Zr-carbide, Zr-nitride and Zr-carbonitride coatings: a review. Mater Adv 2020;1(5):1012–37.

[33] Kuznetsova TA, Andreev MA, Markova LV. Research of wear resistance of the combined vacuum electroarc coatings on the basis of ZrHf. J Frict Wear 2005;26 (5):521–9.

[34] Vereschaka A, Milovich F, Andreev N, Seleznev A, Alexandrov I, Muranov A, et al. Comparison of properties of ZrHf-(Zr,Hf)N-(Zr,Hf,Cr,Mo,Al)N and Ti-TiN-(Ti,Cr,Al) N nanostructured multilayer coatings and cutting properties of tools with these coatings during turning of nickel alloy. J Manuf Process 2023;88:184–201.

[35] Vereschaka A, Sitnikov N, Volosova M, Seleznev A, Sotova C, Bublikov J. Investigation of properties of the Zr,Hf-(Zr,Hf)N-(Zr,Hf,Me,Al)N coatings, where me means Cr, Ti, or Mo. Coatings 2021;11(12):1471.

[36] Grigoriev S, Vereschaka A, Uglov V, Milovich F, Tabakov V, Cherenda N, et al. Influence of the tribological properties of the Zr,Hf-(Zr,Hf)N-(Zr,Me,Hf,Al)N coatings (where Me is Mo, Ti, or Cr) with a nanostructured wear-resistant layer on their wear pattern during turning of steel. Wear 2023;518–519:204624.

[37] Wang S-S, Xia Y, Zhang L-B, Guang H-B, Shen M, Zhang F-M. Effect of NbN and ZrN films formed by magnetron sputtering on Ti and porcelain bonding. Surf Coating Technol 2010;205(7):1886–91.

[38] Ramoul C, Beliardouh NE, Bahi R, Nouveau C, Djahoudi A, Walock MJ. Surface performances of PVD ZrN coatings in biological environments. Tribol Mater Surface Interfac 2019;13(1):12–9.

[39] Zambrano DF, Hernández-Bravo R, Ruden A, Espinosa-Arbelaez DG, González-Carmona JM, Mujica V. Mechanical, tribological and electrochemical behavior of Zr-based ceramic thin films for dental implants. Ceram Int 2023;49(2):2102–14.

[40] Corona-Gomez J, Sandhi KK, Yang Q. Wear and corrosion behaviour of nanocrystalline TaN, ZrN, and TaZrN coatings deposited on biomedical grade CoCrMo alloy. J Mech Behav Biomed 2022;130:105228.

[41] Tarek AHJ, Lai CW, Razak BA, Wong YH. Physical vapour deposition of Zr-based nano films on various substrates: a review. Curr Nanosci 2022;18(3):347–66.

[42] Xin Y, Liu C, Huo K, Tang G, Tian X, Chu PK. Corrosion behavior of ZrN/Zr coated biomedical AZ91 magnesium alloy. Surf Coating Technol 2009;203:2554–7.

[43] Ningshen S, Gupta RK, Kamal S, Chawla V, Chandra R, Mudali UK. Corrosion study of ZrN deposited on 304L stainless steel. Surf Eng 2013;29(4):264–70.

[44] Menghani J, Pai KB, Totlani MK. Corrosion and wear behaviour of ZrN thin films. Tribol Mater Surface Interfac 2011;5:122–8.

[45] Zhang S, Wang J, Wu R, Liu L, Pan B, Liu C. Structural and corrosion resistance properties of sputtered zirconium nitride thin films as electrode material for supercapacitor. J Alloys Compd 2022;900:163506.

[46] Jin W, Zhou H, Li J, Ruan Q, Li J, Peng X, et al. Zirconium-based nanostructured coating on the Mg-4Y-3Re alloy for corrosion retardation. Chem Phys Lett 2020; 756:137824.

[47] Blanco D, Viesca JL, Mallada MT, Ramajo B, González R, Battez AH. Wettability and corrosion of [NTf2] anion-based ionic liquids on steel and PVD (TiN, CrN, ZrN) coatings. Surf Coating Technol 2016;302:13–21.

[48] Mansfeld F. The polarization resistance technique for measuring corrosion currentsFontana G, Staehle RW, editors. Adv Corrosion Sci Technol 1976;6(2):163. N.Y.: Plenum Press.

[49] Rybalka KV, Beketaeva LA, Davydov AD. Estimation of corrosion current by the analysis of polarization curves: electrochemical kinetics mode. Russ J Electrochem 2014;50:108–13.

[50] Poorqasemi E, Abootalebi O, Peikari M, Haqdar F. Investigating accuracy of the Tafel extrapolation method in HCl solutions. Corrosion Sci 2009;51(5):1043–54.

[51] Wu ZT, Qi ZB, Zhang DF, Wang ZC. Microstructure, mechanical properties and oxidation resistance of (Zr, Hf)Nx coatings by magnetron co-sputtering. Surf Coating Technol 2015;276:219–27.

[52] Atar E, Kayali ES, Cimenoglu H. The effect of oxidation on the structure and hardness of (Zr, Hf)N coatings. Defect Diffusion Forum 2010;297–301:1395–9.

[53] Standard specification for wrought titanium-6aluminum-4vanadium alloy for surgical implant applications (UNS R56400). West Conshohocken, United States: ASTM International; 2015.

[54] Grigoriev S, Vereschaka A, Zelenkov V, Sitnikov N, Bublikov J, Milovich F, et al. Investigation of the influence of the features of the deposition process on the structural features of microparticles in PVD coatings. Vacuum 2022;202:111144.

[55] Grigoriev S, Vereschaka A, Milovich F, Andreev N, Bublikov J, Seleznev A, et al. Influence of Mo content on the properties of multilayer nanostructured coatings based on the (Mo,Cr,Al)N system. Tribol Int 2022;174:107741.

[56] Grigoriev S, Vereschaka A, Milovich F, Migranov M, Andreev N, Bublikov J, et al. Investigation of the tribological properties of Ti-TiN-(Ti,Al,Nb,Zr)N composite coating and its efficiency in increasing wear resistance of metal cutting tools. Tribol Int 2021;164:107236.

[57] Grigoriev S, Vereschaka A, Uglov V, Milovich F, Tabakov V, Cherenda N, et al. Influence of the tribological properties of the Zr,Hf-(Zr,Hf)N-(Zr,Me,Hf,Al)N coatings (where Me is Mo, Ti, or Cr) with a nanostructured wear-resistant layer on their wear pattern during turning of steel. Wear 2023;518–519:204624.

[58] Vereschaka A, Grigoriev S, Sitnikov N, Milovich F, Aksenenko A, Andreev N. Investigation of performance and cutting properties of carbide tool with nanostructured multilayer Zr-ZrN-$(Zr_{0.5},Cr_{0.3},Al_{0.2})$N coating. Int J Adv Manuf Technol 2019;102(9–12):2953–65.

[59] Grigoriev SN, Vereschaka AA, Fyodorov SV, Sitnikov NN, Batako AD. Comparative analysis of cutting properties and nature of wear of carbide cutting tools with multi-layered nano-structured and gradient coatings produced by using of various deposition methods. Int J Adv Manuf Technol 2017;90:3421–35.

[60] Vereschaka A, Tabakov V, Grigoriev S, Sitnikov N, Milovich F, Andreev N, et al. Investigation of the influence of the thickness of nanolayers in wear-resistant layers of Ti-TiN-(Ti,Cr,Al)N coating on destruction in the cutting and wear of carbide cutting tools. Surf Coat Technol 2020;385:125402.

[61] Standard test method for wear testing with a pin-on-disk Apparatus (G 99 – 95a). West Conshohocken, United States: ASTM International; 2000.

[62] Standard test method for adhesion strength and mechanical failure modes of ceramic coatings by quantitative Single point scratch testing (C1624 – 05). West Conshohocken, United States: ASTM International; 2010.

[63] Jin W, Wu G, Li P, Chu PK. Improved corrosion resistance of Mg-Y-RE alloy coated with niobium nitride. Thin Solid Films 2014;572:85–90.

[64] Vereschaka A, Tabakov V, Grigoriev S, Sitnikov N, Milovich F, Andreev N, et al. Investigation of wear dynamics for cutting tools with multilayer composite nanostructured coatings in turning constructional steel. Wear 2019;420–421: 17–37.

[65] Vereschaka AA, Grigoriev SN. Study of cracking mechanisms in multi-layered composite nano-structured coatings. Wear 2017;378–379:43–57.

[66] Li R, Wang S, Zhou D, Pu J, Yu M, Guo W. A new insight into the NaCl-induced hot corrosion mechanism of TiN coatings at 500 °C. Corrosion Sci 2020;174:108794.

[67] Zhang MM, Xin L, Ding XY, Zhu SL, Wang FH. Effects Ti/TiAlN composite multilayer coatings on corrosion resistance of titanium alloy in solid NaCl-H_2O-O_2 at 600 °C. J Alloys Compd 2017;734:307–17.